

# Double-Layer Graphene Outperforming Monolayer as Catalyst on Silicon Photocathode for Hydrogen Production

Uk Sim,<sup>†,⊥</sup> Joonhee Moon,<sup>‡,||,⊥</sup> Joohee Lee,<sup>†</sup> Junghyun An,<sup>†</sup> Hyo-Yong Ahn,<sup>†</sup> Dong Jin Kim,<sup>§</sup> Insu Jo,<sup>‡</sup> Cheolho Jeon,<sup>||</sup> Seungwu Han,<sup>†</sup> Byung Hee Hong,<sup>\*,‡,§</sup> and Ki Tae Nam<sup>\*,†,⊥</sup>

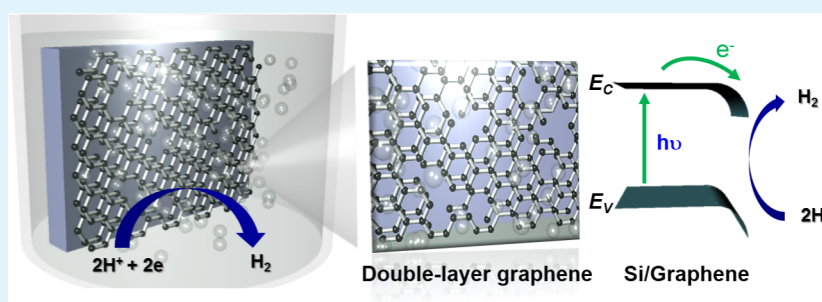
<sup>†</sup>Department of Materials Science and Engineering, Seoul National University, Seoul 08 826, Republic of Korea

<sup>‡</sup>Department of Chemistry, Seoul National University, Seoul 08 826, Republic of Korea

<sup>§</sup>Department of Nano Science and Technology, Graduate School of Convergence Science and Technology, Seoul National University, Seoul 08 826, Republic of Korea

<sup>||</sup>Korea Basic Science Institute, Gwahangno, Yuseong-gu, Daejeon, 305-333, Korea

## Supporting Information



**ABSTRACT:** Photoelectrochemical cells are used to split hydrogen and oxygen from water molecules to generate chemical fuels to satisfy our ever-increasing energy demands. However, it is a major challenge to design efficient catalysts to use in the photoelectrochemical process. Recently, research has focused on carbon-based catalysts, as they are nonprecious and environmentally benign. Interesting advances have also been made in controlling nanostructure interfaces and in introducing new materials as catalysts in the photoelectrochemical cell. However, these catalysts have as yet unresolved issues involving kinetics and light-transmittance. In this work, we introduce high-transmittance graphene onto a planar p-Si photocathode to produce a hydrogen evolution reaction to dramatically enhance photon-to-current efficiency. Interestingly, double-layer graphene/Si exhibits noticeably improved photon-to-current efficiency and modifies the band structure of the graphene/Si photocathode. On the basis of in-depth electrochemical and electrical analyses, the band structure of graphene/Si was shown to result in a much lower work function than Si, accelerating the electron-to-hydrogen production potential. Specifically, plasma-treated double-layer graphene exhibited the best performance and the lowest work function. We electrochemically analyzed the mechanism at work in the graphene-assisted photoelectrode. Atomistic calculations based on the density functional theory were also carried out to more fully understand our experimental observations. We believe that investigation of the underlying mechanism in this high-performance electrode is an important contribution to efforts to develop high-efficiency metal-free carbon-based catalysts for photoelectrochemical cell hydrogen production.

**KEYWORDS:** silicon, graphene, hydrogen evolution reaction (HER), metal free catalyst, photoelectrochemical cell

## INTRODUCTION

The realization of cost-effective water-splitting for hydrogen production requires photoelectrochemical cells (PECs) with highly efficient cocatalysts.<sup>1–5</sup> In the race to replace noble-metal catalysts, carbon-based nanomaterials have emerged as promising candidates for producing the hydrogen evolution reaction (HER).<sup>6</sup> We are the first to investigate the use of monolayer graphene as an electrocatalyst for efficient HER, employing a Si substrate as a photocathode.<sup>7</sup> We prepared mono-, double-, tri-, and multilayer graphene on p-Si photocathodes and investigated the layer dependence of catalytic activity for HER. A comprehensive electrochemical

analysis proved that a heterojunction between the Si semiconductor, graphene layer, and electrolyte play a pivotal role in determining catalytic activity and PEC performance. After analyzing the junction effect, we found that plasma-treated double-layer graphene was the best of all graphene catalysts reported to date in terms of PEC activity and charge-transfer rate in the HER.

**Received:** September 15, 2016

**Accepted:** January 11, 2017

**Published:** January 11, 2017

Carbon-based nanomaterials have attracted considerable attention as low cost, highly stable catalytic materials for a variety of chemical reactions, such as the HER,<sup>8</sup> the oxygen evolution reaction,<sup>9</sup> and the oxygen reduction reaction.<sup>10</sup> N and P heteroatoms adjacent to C atoms in the graphene matrix can affect these catalysts' valence orbital energy levels, thereby enhancing their reactivity in the HER.<sup>6</sup> Graphitic-carbon nitride combined with nitrogen-doped graphene also exhibits enhanced HER activity with properties similar to those of well-established metallic catalysts.<sup>11</sup> Certain materials loaded onto reduced graphene oxide have exhibited improved catalytic activity in oxygen-reduction reactions and oxygen-evolution reactions as well as in the HER.<sup>10,12–16</sup> In most cases, however, the role of carbon materials has been limited to use as an electrically conductive substrate, or to promote the activity of other metal-based cocatalysts in photoelectrochemical properties.<sup>10,12,13</sup>

Graphene, an ultrathin, flat monolayer of carbon atoms, continues to attract extensive interest because of its outstanding electronic and structural properties, which make it a promising candidate for touch-screen displays,<sup>17</sup> photonics, and optoelectronics,<sup>18</sup> and energy storage systems.<sup>19–23</sup> In our previous reports, a graphene-silicon electrode was found to be effective for the HER because of its superior transmittance, oxidation barrier, and abundant reaction sites for electron transfer.<sup>7,24,25</sup> In another study, we treated graphene with nitrogen plasma to increase the number of active sites, including doping sites and defect sites to enhance the HER, and proposed nitrogen-doped graphene quantum sheets (N-GQs) and silicon nanowires to further improve efficiency through orthogonalization of incidental light absorption and charge carrier collection. The combination of optimized Si nanowires and N-GQs showed an applied bias photon-to-current efficiency (ABPE) of 2.29%. This finding led us to believe that the introduction of graphene and N-GQs as high-performance, low-cost electrodes with superior cycle stability would constitute an important breakthrough for the HER and for future energy-storage systems.

Recently, various multilayer graphene structures have been used in efforts to alter the physical and chemical properties of catalysts and active electrode materials. However, studies are still needed to understand the interaction between multilayer graphene structures and Si substrates. Graphene has striking electrical,<sup>26,27</sup> chemical,<sup>28</sup> and optical properties.<sup>17</sup> Graphene is an interesting material because layers of graphene can be stacked and counted and the number of graphene layers can affect the voltage of solar cells.<sup>29</sup> Yeom's group reported that the photovoltaic response of graphene/Si is directly dependent upon the number of graphene layers and that the power-conversion efficiencies of devices with mono- and double-layer graphene structures are higher than those of devices with tri- and tetra-layer graphene.<sup>29</sup> Moreover, carrier mobility decreases in monolayer graphene as temperature increases, due to surface polar photon scattering, while the carrier mobility of double- and trilayer-graphene is higher because scattering is screened by the additional graphene layers.<sup>30</sup> Lee's group calculated the interaction between graphene and H-passivated Si(100) and found that the change in band gap was negligible in monolayer graphene.<sup>31</sup> The electronic properties of double-layer graphene on Si(100) changed significantly because of asymmetry in carbon sites, which caused band gap widening as much as 108 meV.

The electrochemical behavior of graphene, graphene multilayers, and graphene derivatives has been the subject of much

recent study, with seemingly inconsistent findings. Monolayer and double-layer graphene microelectrodes have been shown to have one to two times faster electron transfer kinetics for ferricyanide reduction compared to the transfer kinetics of multilayer basal plane graphitic substrates, and defects in monolayer graphene exerted only minimal influence on voltammetric response.<sup>32</sup> In contrast, Dale et al. have reported that monolayer graphene electrodes possess slow heterogeneous electron transfer (HET) kinetics compared to electrodes with on average four layers of graphene, which they refer to as quasi-graphene electrodes, and which demonstrated a two to eight times faster transfer rate. They attributed this to monolayer graphene's low degree of edge-plane coverage.<sup>33</sup> In other research, the HET properties of multilayer graphene film transferred onto an insulating polyethylene terephthalate substrate have also been investigated using various redox mediators.<sup>34</sup> These properties were found to be similar to those of basal-plane graphite with low density edge-plane defect sites.

Electrochemical research on graphene has been relatively limited. The electrochemical properties of monolayer or multilayer graphene have mostly been investigated in terms of HET and have been compared with those of heterogeneous graphitic surfaces at edge-plane sites or on the basal plane. Other research has focused on the electrochemical behavior of monolayer graphene-coated n-type Si(111) photoanodes only as a passivation layer formed by oxidation in an aqueous solution, finding that coating with a single layer of graphene increased stability at high light intensity.<sup>35</sup> Unfortunately, studies on PEC responses specifically attributable to the number of graphene layers on electronic structures in a heterojunction system are lacking.

Here, we elucidate the mechanism of the PEC response for HER at the interface between graphene and the Si substrate. In our study, graphene was selectively controlled layer-by-layer via an advanced graphene transfer-technique that we developed. We also introduced plasma treatment onto variously layered graphene to generate more active sites. The graphene was synthesized via chemical vapor deposition (CVD) and randomly oriented in a layer-by-layer transfer. The work function of the plasma-treated double-layer graphene on the Si electrode unexpectedly yielded the smallest value and induced the strongest band bending for enhanced HER, consistent with the results of a Mott–Schottky analysis at the interface between the graphene/Si and the electrolyte. Moreover, the PEC performance exhibited enhanced efficiency of 0.32%, which is 64 times higher than that of bare Si and is the highest value recorded for carbon-based catalysts on planar p-Si photocathodes.

## RESULTS AND DISCUSSION

Figure 1 shows the HER using a double-layer graphene coating on p-type Si in an acidic solution under irradiation. Photons absorbed by the silicon wafer generated minority carriers (electrons), which were diffused onto the graphene at the semiconductor/electrolyte interface, reducing  $2\text{H}^+$  to  $\text{H}_2$ . The double-layer graphene played a key role not only as an electrocatalyst for HER but also in tuning the surface work function of the photocathode to facilitate hydrogen gas generation. Figure 2a–d shows atomic force microscope (AFM) images showing that as the number of layers increases, there is also a gradual increase in surface roughness, wrinkles, and folded regions. The inset shows the height profile of each graphene layer: the thickness of monolayer graphene was less

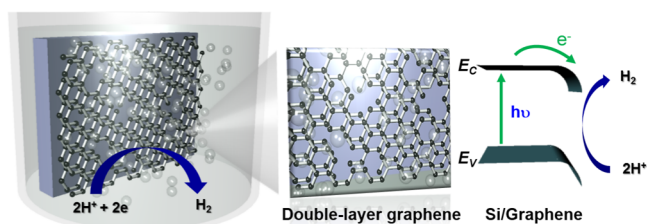


**Figure 1.** Schematic of double-layer graphene on p-silicon photocathode. Minor carriers (electrons) are generated when silicon absorbs photons, which are diffused to the photocathode/electrolyte interface, where  $2\text{H}^+$  is reduced to  $\text{H}_2$ . Plasma-treated double-layer graphene acts as an electrocatalyst for hydrogen production as well as induces surface modification of the photocathode leading to changes in the energy band diagram of the photocathode.  $E_{\text{CB}}$  and  $E_{\text{VB}}$  indicate conduction band maximum and valence band minimum of the graphene/Si photocathode. The photogenerated electron can be easily moved to the conduction band edge of graphene/Si, and strong band bending accelerates hydrogen production.

than 1 nm, double-layer graphene was approximately 1.5 nm, trilayer graphene was less than 3 nm, and multilayer (4 layer) graphene was approximately 4 nm because of wrinkles and folded areas. Focused ion beam milling was used to prepare transmission electron microscopy (TEM) specimens in order

to study the interfacial structure between the graphene and Si electrode. The cross-sectional TEM images show that mono-, double-, tri-, and multilayer graphene transferred well onto the Si electrode; a partially folded area is shown in Figure 2e–h. The typical-real-space TEM images of the various graphene structures show largely clean and flat layers. Each inset represents the fast Fourier transform (FFT) of each image. The inset of Figure 2i shows six diffraction spots of the same intensity, exhibiting the classic pattern of monolayer graphene. The two sets of hexagonal patterns in the double-layer graphene were rotated relative to each other by  $\sim 23.5^\circ$ . From the diffraction spots, we were able to confirm that the upper and lower graphene layers were stacked at rotated angles. The three sets of patterns in the differentiation spots in the trilayer graphene and the four sets in the multilayer graphene also then indicate that the transfer of each graphene layer resulted in some rotation. To verify the graphene layers as graphene and the degree of crystallinity, a Renishaw spectrometer at 514 nm was used to conduct Raman spectroscopy at room temperature on each graphene on silicon oxide sample (Figure 2m). The two most pronounced peaks were the G peak at  $1590\text{ cm}^{-1}$  and 2D peak at  $2700\text{ cm}^{-1}$ , which originated from the in-plane vibrational  $E_{2g}$  phonon and the second order of zone-boundary phonons, respectively.<sup>36</sup> Additionally, the D peak was detected in the breathing mode of

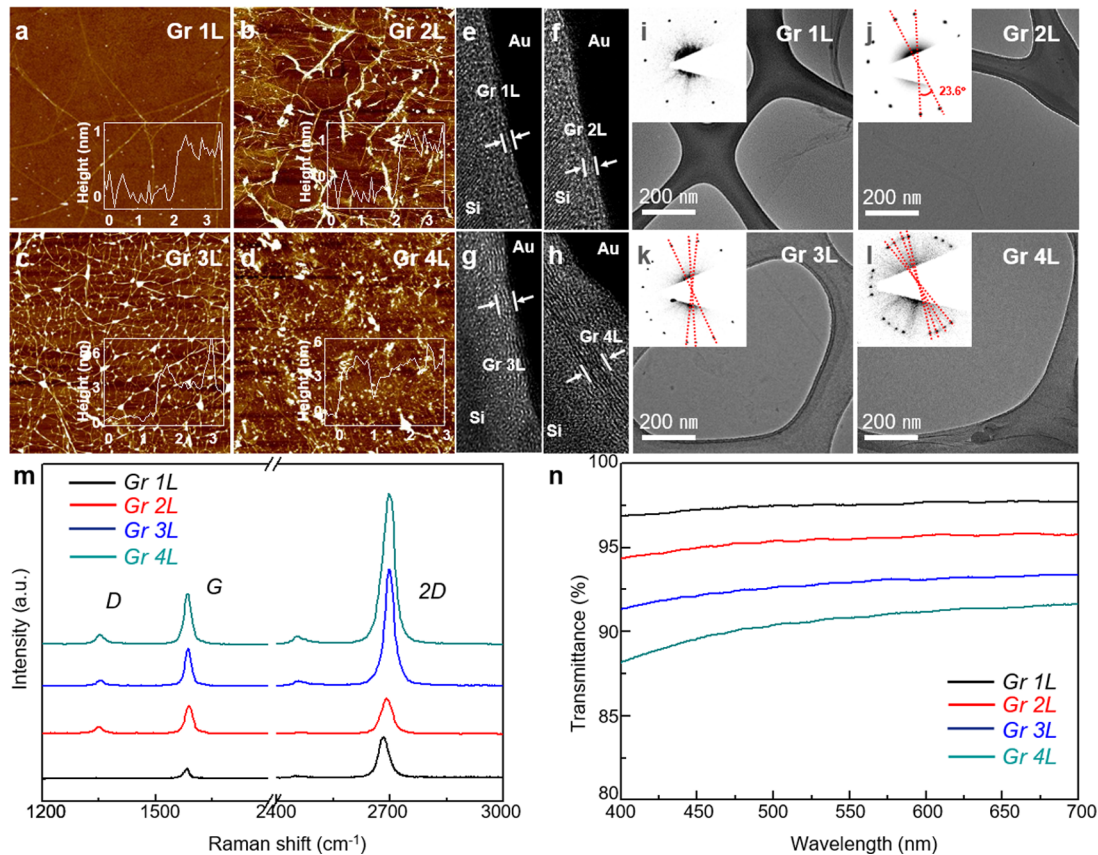


**Figure 2.** Surface characterization of graphene according to number of layers. (a–d) Atomic force microscopy (AFM) images of graphene with different numbers of layers: monolayer graphene (Gr 1L), double-layer graphene (Gr 2L), trilayer graphene (Gr 3L), and multilayer graphene (Gr 4L). The scan size:  $10 \times 10\ \mu\text{m}^2$ . Each inset shows the height profile. (e–h) Cross-sectional TEM images of graphene with different numbers of layers on Si electrode and (i–l) top-view TEM images of graphene with different numbers of layers on holly carbon grid. Each inset shows the selective area electron diffraction (SAED) of each image. The hexagonal patterns in double-, tri-, and multilayer graphene show that graphene layers are misaligned when the graphene is transferred and stacked. (m) Raman spectra of graphene with different numbers of layers. (n) Transmittance of graphene specimens on polyethylene terephthalate substrate.

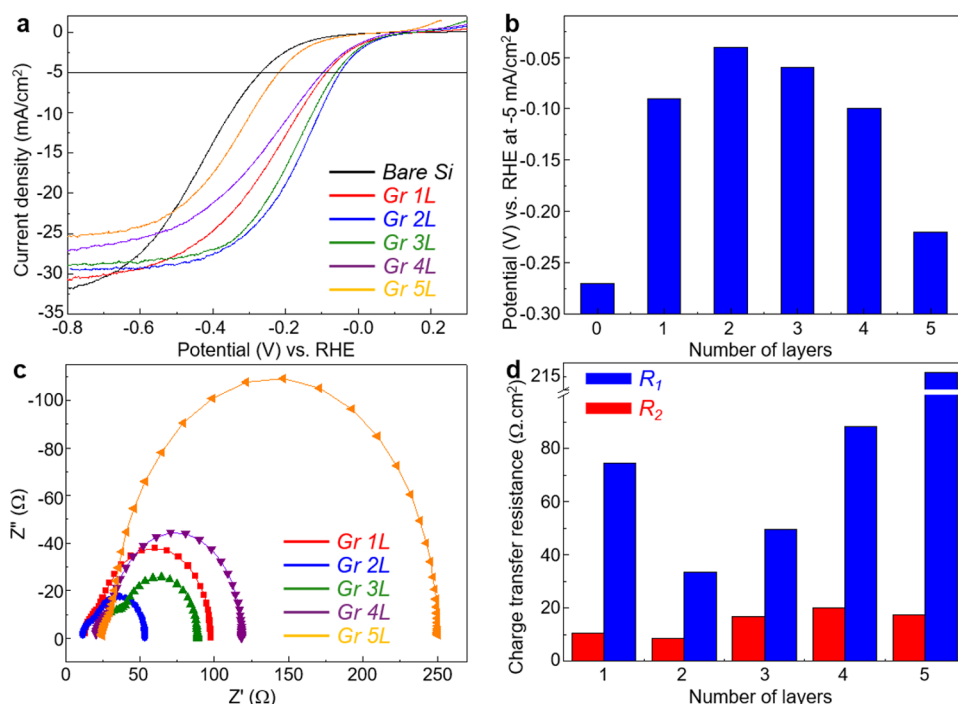


**Figure 3.** Photoelectrochemical response of graphene on silicon. (a) Photocurrent density-potential ( $J$ - $E$ ) curves of multiple layers of graphene on lightly boron-doped planar p-Si. (b) Potential vs RHE at  $-5 \text{ mA/cm}^2$  depending on the number of graphene layers. (c) Nyquist plot for graphene/Si electrode at  $0 \text{ V}$  vs RHE under illumination condition. (d) Charge transfer resistance with different numbers of graphene layers.  $R_1$  is the charge transfer resistance of the electrical double layer at the interface between the electrode and electrolyte, and  $R_2$  is the charge transfer resistance of the depletion layer in graphene/Si.

six-atom rings at  $1350 \text{ cm}^{-1}$ , which is negligibly weak in monolayer graphene (approximately 5% of the G peak intensity in this paper). The absence of a significant D peak is evidence of good crystallization of the monolayer graphene. With the transfer of each graphene layer, the intensities of both the G- and 2D-band peaks increased, and the 2D peaks became slightly blue-shifted relative to the 2D peak in monolayer graphene. However, the intensity ratio of the G peak to the 2D peak ( $I_G/I_{2D}$ ) did not change significantly. We observed a D peak at  $1350 \text{ cm}^{-1}$  in the several-layer graphene specimens, which indicated the presence of defects in the upper and lower layers that were most likely introduced by randomly oriented hexagonal lattices, which are not present in the structure of graphite. Spatially resolved Raman maps of different numbers of layers of graphene were also obtained and analyzed to investigate the uniform morphology of graphene (Figure S2 of the Supporting Information). Each of the Raman mapping images is plotted using an Intensity 2D peak,  $I(2D)$ , which shows the uniform surface morphology of the graphene layers. Therefore, the properties of each graphene layer remained unchanged, even after stacking. In contrast, the optical transmittance of each graphene on polyethylene terephthalate (PET) sample was reduced by approximately 2.3% for each additional layer, which reduced the transmittance of multilayer graphene (4 layers) to 90% transmittance at 550 nm. The superior transmittance of graphene substantially enhanced the amount of incident light reaching the photocathode.

The PEC performance of graphene/Si electrodes for hydrogen production is strongly dependent on the number of graphene layers. To evaluate the photocathodic behavior of graphene/Si electrodes, photocurrent density was measured by performing linear sweep voltammetry, sweeping from positive to negative potential from  $0.3 \text{ V}$  to  $-0.8 \text{ V}$  with a reversible

hydrogen electrode (RHE) as the reference electrode. As shown in Figure 3a, the photocurrent density of bare planar Si increased gradually starting at  $-0.2 \text{ V}$  measured with respect to the RHE, and became saturated at a current density of approximately  $-31 \text{ mA/cm}^2$  at the specific applied potential of  $-1.0 \text{ V}$  vs RHE. Measurement of monolayer graphene on planar Si showed that the potential required to attain a current density of  $-5 \text{ mA/cm}^2$  was  $180 \text{ mV}$  more positive than that for bare planar Si. When graphene layers were added on the electrode, up to five layers in total, all samples showed positive shifts in the overall photocurrent density-potential ( $J$ - $E$ ) response curve. Interestingly, the  $J$ - $E$  curve for double-layer graphene showed the largest positive shift. The potential at  $-5 \text{ mA/cm}^2$  was  $-0.04 \text{ V}$  vs RHE, indicating a positive shift of  $230 \text{ mV}$  compared to bare Si ( $-0.27 \text{ V}$  vs RHE). Thereafter, the potential at  $-5 \text{ mA/cm}^2$  decreased with additional graphene layers (Figure 3b). To compare incident photon-to-current conversion efficiency, the applied bias photon-to-current efficiency (ABPE) was calculated from the  $J$ - $E$  response using the following formula:<sup>37</sup>

$$\text{ABPE} = \left[ \frac{j_{\text{ph}} (\text{mA/cm}^2) \times (V_{\text{redox}} - V_{\text{bias}}) (\text{V})}{P_{\text{in}} (\text{mW/cm}^2)} \right]_{\text{AM1.5G}} \times 100 (\%) \quad (1)$$

where  $j_{\text{ph}}$  is the photocurrent density obtained under an applied bias  $V_{\text{bias}}$ ,  $V_{\text{redox}}$  is the redox potential for hydrogen production ( $0 \text{ V}$ ),  $V_{\text{bias}}$  is the externally applied bias potential that is often necessary to achieve reasonable photocurrents, and  $P_{\text{in}}$  is the intensity of the incident light in the AM 1.5 G condition ( $100 \text{ mW/cm}^2$ ). Figure S3 and Table S1 summarize the efficiency data for various catalysts on p-type planar Si photocathodes. When double-layer graphene was deposited on the Si, the conversion efficiency was 0.05%, ten times higher than with

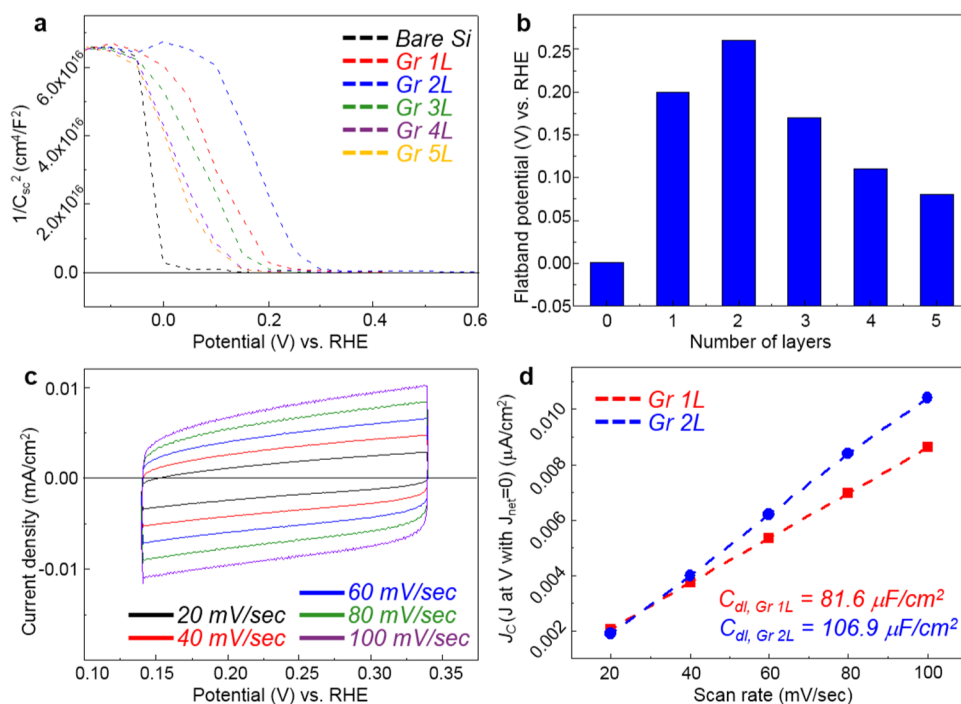


**Figure 4.** Electrochemical response of graphene on silicon under dark conditions. (a) Mott–Schottky plots of bare Si and graphene on Si from capacitance measurement as a function of potential vs RHE under dark conditions.  $C_{sc}$  is the capacitance of the space charge region. (b) Flatband potential of graphene with different numbers of graphene layers. (c) The current to potential result of monolayer graphene on Si electrode at different scan rates. (d) The capacitance current ( $J_c$ ) of mono- and double-layer graphene at  $J_{net} = 0$  mA/at different scan rates. The slope of the  $J_c$  to scan rates plot is the capacitance of the double-layer graphene ( $C_{dl}$ ).

bare Si, and 1.25 times higher than with monolayer graphene on Si (Figure S4). Both the double-layer and monolayer graphene coatings served as effective HER catalysts on the Si photocathode. However, the transfer of additional graphene layers gradually decreased conversion efficiency. As shown in Figure 3a, the saturation current density decreased from 31.1 mA/cm<sup>2</sup> to 24.9 mA/cm<sup>2</sup> as the number of graphene layers increased. A decrease in the current density of approximately 97.7% with each graphene layer closely corresponds to the intrinsic optical transmittance of the graphene layer (Figure 2n), which also decreased by approximately 97.7% for each layer (Figure S4). The observed decrease in saturation current density can be attributed to decreased light absorption. Thus, we conclude that the number of graphene layers significantly affects light absorption, which in turn affects PEC performance. Chronoamperometry tests on bare Si and on graphene layers on Si electrodes were performed at 0 V vs RHE and current densities normalized by their initial values were displayed as a function of time in Figure S5. Graphene layers on Si electrodes showed greater suppression of photocurrent density performance degradation compared to bare Si. The performance of bare Si significantly decreased only after 2000 s. However, most graphene layers on Si electrodes maintained between 27% and 38% of the normalized current even at 12,000 s except for the structure with five layers of graphene on Si. This result indicates that the graphene layers also exhibit good stability, demonstrating the significance of the practical application of graphene layers to silicon-based photoelectrochemical hydrogen production. To investigate the cause of change in catalytic activity based on the number of graphene layers, electrochemical impedance measurements were performed. Figure 3c shows semicircles on a Nyquist plot representing typical impedance for different numbers of layers of graphene on Si electrode.

Impedance is related to charge-transfer resistance, so that the semicircles shown in Figure 3c all suggest much lower charge-transfer resistance than the known charge-transfer resistance for bare Si (not shown in the figure). Graphene/Si electrodes show two semicircles, corresponding to two different charge-transfer resistances:  $R_1$  and  $R_2$  (see Experimental Section). Charge transfer across the electrical double layer at the semiconductor/electrolyte interface was dominant in the low-frequency region, while in the depletion layer of the semiconductor, more charge transfer occurred in the high-frequency region.<sup>37,38</sup> In the case of double-layer graphene/Si electrodes, both semicircles are smaller than those for the other graphene/Si structures, and thus, the values of both  $R_1$  and  $R_2$ , i.e., the overall charge-transfer resistance, for double-layer graphene/Si electrodes were the lowest of all the graphene/Si electrodes, as shown in Figure 3d and Table S2. Charge-transfer resistance is related to the kinetic energy needed to overcome the energy barrier for faradaic reactions across the electrical double layer.<sup>38</sup> Charge-transfer resistance is also inversely proportional to the exchange current density in the faradaic reaction, as described in the Butler–Volmer equation.<sup>39</sup> A graphene/Si structure with a lower charge-transfer resistance promotes the faradaic reaction, which is related to a relatively low  $R_1$  value, thus enhancing HER (through faradaic reactions) and lowering overpotential. The smaller semicircle in the high-frequency range (related to  $R_2$ ) indicates that the charge-transfer resistance of the semiconductor depletion layer in the graphene/Si is also lower than that of bare Si. This depletion layer resistance is also correlated to a higher photocurrent response because of increased band bending in the depletion layer.<sup>40,41</sup>

To study the band bending effect of the graphene layers on the Si electrode in an aqueous electrolyte, capacitance measurements were performed as the applied potential was

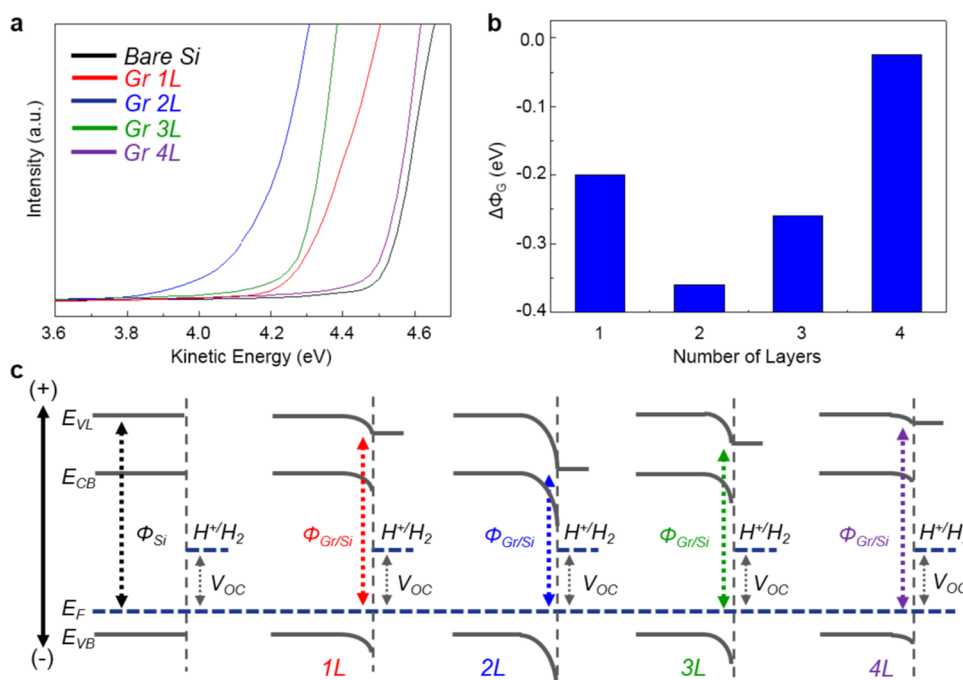


**Figure 5.** Work function and energy band diagrams with different numbers of graphene layers/Si. (a) Ultraviolet photoelectron spectroscopy (UPS) spectra of mono-, bi-, tri-, and multilayer graphene on Si electrode. (b) Work function difference ( $\Delta\Phi_G$ ) between graphene and Si with different numbers of graphene layers. (c) Schematic energy band diagrams of bare Si and graphene/Si on the basis of the work function values measured by UPS.  $E_{VL}$ ,  $E_{CB}$ ,  $E_{VB}$ ,  $E_F$ , and  $\Phi_{Si}$  represent vacuum level, conduction band edge, valence band edge, Fermi level, and work function of silicon electrode. The difference in  $E_F$  and  $H^+/H_2$  is the maximum attainable photovoltage ( $V_{OC}$ ).

swept from 0.6 V to  $-0.3$  V vs RHE at a frequency of 1000 Hz in a three-electrode cell without illumination, as shown in Figure 4a. The flat-band potential of bare Si and graphene/Si electrodes were calculated from the capacitance results using the Mott–Schottky relationship:<sup>42</sup>

$$1/C_{sc}^2 = 2(E - E_{fb} - kT/e)/(e\epsilon\epsilon_0N) \quad (2)$$

where  $C_{sc}$  is the capacitance of the space charge region,  $\epsilon$  is the dielectric constant of the semiconductor,  $\epsilon_0$  is the permittivity of free space,  $N$  is donor density (i.e., the hole acceptor concentration for a p-type semiconductor),  $E$  is applied potential, and  $E_{fb}$  is flat-band potential. Figure 4a shows typical Mott–Schottky plots for a p-type silicon semiconductor. Donor density was calculated from the slope, and the  $E_{fb}$  was determined by extrapolation to a capacitance of zero. The monolayer graphene/Si electrode exhibited an  $E_{fb}$  of 0.20 V vs RHE, whereas the  $E_{fb}$  of the bare planar Si was 0.001 V vs RHE, as shown in Figure 4b. The applied potential and  $E_{fb}$  determine the magnitude of band bending in the semiconductor ( $E_b$ ) according to the equation:  $E_b = E - E_{fb}$ .<sup>43</sup> As  $E_{fb}$  increases positively, the absolute value of  $E_b$  increases because the applied potential  $E$  is always negative for proton reduction at the cathode. Higher band bending at the electrode/electrolyte interface promotes faster charge separation of generated electrons and holes.<sup>40</sup> The higher  $E_{fb}$  of the graphene/Si electrode relative to that of the bare planar Si appears to have increased the extent of band bending at the depletion region of the semiconductor near the solid/solution interface because of the relationship between  $E_b$  and  $E_{fb}$ . Furthermore, in the case of double-layer graphene/Si,  $E_{fb}$  increased to 0.26 V vs RHE, which was the strongest band bending among all of the multilayered graphene/Si electrode structures. Meanwhile, the doping densities of bare Si and graphene/Si were calculated

from the Mott–Schottky relationship. Using eq 2, bare Si was calculated to have a donor density of  $4.46 \times 10^{15} / \text{cm}^3$ , whereas graphene/Si electrodes had an average donor density of  $5.74 \times 10^{15} / \text{cm}^3$ . Interestingly, transferring additional graphene layers had little influence on the value of the slope. Another assumption is that the intrinsic catalytic activity of graphene might also have influence on interface and band bending. We measured the dark current of graphene on a p-type silicon electrode. As shown in Figure S6, double-layer graphene showed the highest current density as the cathodic potential increased, which tendency is the same as for a graphene/Si structure under illumination. To further confirm the electrocatalytic activity of the graphene layers, we also measured dark current densities of graphene layers on a glassy carbon electrode, the standard electrode for evaluation of HER properties. We found that graphene layers on a glassy carbon electrode showed higher current density after onset potential compared to a bare glass carbon electrode (Figure S7). The potential at  $10 \text{ mA/cm}^2$  is  $-0.26$  V vs RHE, which is comparable to other metal-free carbon-based catalysts.<sup>11</sup> These results show that graphene layers have intrinsic catalytic properties and strongly influence interface and band bending. To gain more insight into the effect of the number of graphene layers, we also investigated (1) cyclic voltammetry (CV) scan-rate dependence to confirm the capacitance of the electrical double layer at the solid/solution interface and (2) the UV photoelectron spectroscopy (UPS) characterization to investigate the source of the change in the depletion region of graphene/Si.

The capacitance of the electrical double layer at the solid/solution interface was evaluated by measuring the  $J$ – $E$  response of the graphene/Si electrode at various scan rates, as shown in Figure 4c. The capacitance of the double layer was estimated

from the slope of the plot of  $J_C$ , which was the current at a potential with a net current density of  $0 \mu\text{A}/\text{cm}^2$ , as a function of the scan rate (Figure 4d). The capacitance of monolayer graphene was  $81.6 \mu\text{F}/\text{cm}^2$ , and that of the double-layer graphene was  $106.9 \mu\text{F}/\text{cm}^2$ , both of which were higher than those of either bare Si ( $10 \mu\text{F}/\text{cm}^2$ ) or a compact flat electrode ( $10\text{--}20 \mu\text{F}/\text{cm}^2$ ).<sup>44</sup> The slope was also proportional to the exchange current density, which was directly related to the catalytically active surface area.<sup>45,46</sup> The graphene layers, therefore, had relatively large electrochemical catalytic surface areas, which should contain intrinsic active sites for the HER. Moreover, double-layer graphene had an electrochemical surface area 1.31 times larger than that of monolayer graphene. The larger surface area of double-layer graphene may have been the result of wrinkles, ripples, or folded areas created when the graphene was transferred. Therefore, more active surface areas for HER were generated in the double-layer graphene.

UPS He I (21.2 eV) was investigated to study the effect of the energy band structure in hydrogen production. Figure 4a shows the onset of the secondary cutoff of the photoemission electron spectra of Si and graphene/Si electrodes. The work function ( $\Phi$ ) was calculated as follows:<sup>29</sup>

$$\Phi = hv - |E_{\text{cut-off}} - E_{\text{F}}| \quad (3)$$

where  $E_{\text{F}}$  is the Fermi level energy, and  $E_{\text{cut-off}}$  is the secondary cutoff energy. The work function of the bare Si substrate, approximately  $4.61 \pm 0.02$  eV, decreased with the addition of graphene layers. These changes are depicted as  $\Delta\Phi_{\text{Gr}}$  in Figure 5b. The  $\Delta\Phi_{\text{Gr}}$  is  $-0.2$  eV for monolayer graphene,  $-0.36$  eV for double-layer graphene,  $-0.26$  eV for trilayer graphene, and  $-0.025$  eV for multilayer graphene (four layers). This result indicates that the work function of graphene/Si electrodes can be controlled by the addition of graphene layers, which also changes the energy band structure of the photoelectrode. Interestingly, double-layer graphene on Si shows the smallest work function. Figure 5c describes the interface energetics between the photocathode and electrolyte, showing the energy bands for bare Si and graphene/Si based on work function values measured by UPS. The difference between  $E_{\text{F}}$  and the  $\text{H}^+/\text{H}_2$  redox potential in the energy band diagram of Si is the maximum attainable photovoltage ( $V_{\text{OS}}$ ), which also represents the maximum amount of band-bending at the bare Si/electrolyte interface. As shown in Figure 5c, the smaller work function at the graphene/electrolyte interface in graphene/Si structures indicates that the conduction band edge is strongly bent to the potential of the  $\text{H}^+/\text{H}_2$  redox couple. As a result, the double-layer graphene/Si has the smallest work function, which results in the strongest band bending in the depletion region, leads to the largest shift in the overall photocurrent response curve, as shown in Figure 3a. The potentials at  $-1 \text{ mA}/\text{cm}^2$ , at  $-5 \text{ mA}/\text{cm}^2$ , and at  $-10 \text{ mA}/\text{cm}^2$  show the highest values among graphene/Si structures (Table S1). The schematic depiction of the work function is also well supported by the results for the flat-band potential from the Mott–Schottky plot, as shown in Figure 4a. The double-layer graphene/Si heterostructure shows the Schottky contact, which produces an electron path for proton reduction at the electrode/electrolyte interface.<sup>29</sup> Bilayer graphene has been reported to cause opening of the band gap, which may affect the work function of the graphene/Si structure.<sup>26</sup> The present results show that surface modification with layered graphene changes band bending of the Si surface and affects the kinetics of hydrogen production.

To analyze the mechanism causing the graphene overlayer to change work function, a computational study based on the density functional theory was conducted (See Experimental Section). The heterostructure of monolayer graphene and p-Si(100) was modeled by expanding unit cells of each structure and applying small distortions of  $\sim 1\%$  (Figure S12a). P-type doping was emulated by inserting one B atom in the middle of the Si slab, corresponding to a doping concentration of  $4 \times 10^{20} \text{ cm}^{-3}$ . The work functions of the B-doped Si slab and the monolayer graphene coating were calculated to be 4.71 and 4.34 eV, respectively, which compares favorably with the experimental values of 4.61 and 4.4 eV.<sup>47</sup> When the Si slab and graphene coating came in contact as shown in Figure S12a, the work function reached 4.45 eV with respect to the vacuum above the graphene: that is to say, the work function was offset by  $-0.26$  eV in the calculation, which is consistent with the experimental value when the monolayer graphene was overlaid.

The charge transfer between graphene and Si was analyzed by calculating the electron redistribution ( $\Delta n(r)$ ) in the heterostructure as follows:

$$\Delta n(\vec{r}) = n_{\text{Si+Gr}}(\vec{r}) - n_{\text{Si}}(\vec{r}) - n_{\text{Gr}}(\vec{r}) \quad (4)$$

where,  $n(r)$  indicates the electron density for each system. The  $xy$ -averaged electron transfer ( $\Delta n(z)$ ) is obtained as follows:

$$\Delta n(z) = \frac{1}{A} \int_A \Delta n(\vec{r}) \, dx dy \quad (5)$$

where  $A$  is the area of the surface unit cell. The computed  $\Delta n(z)$  is displayed in Figure 6b. It is seen that the electron is transferred from double-layer graphene to the Si side at the interface region. The resulting Coulombic shift was computed to be  $-0.21$  eV, which explains the theoretical change in the work function. Therefore, we conclude that the work function change is mainly due to the charge transfer between graphene

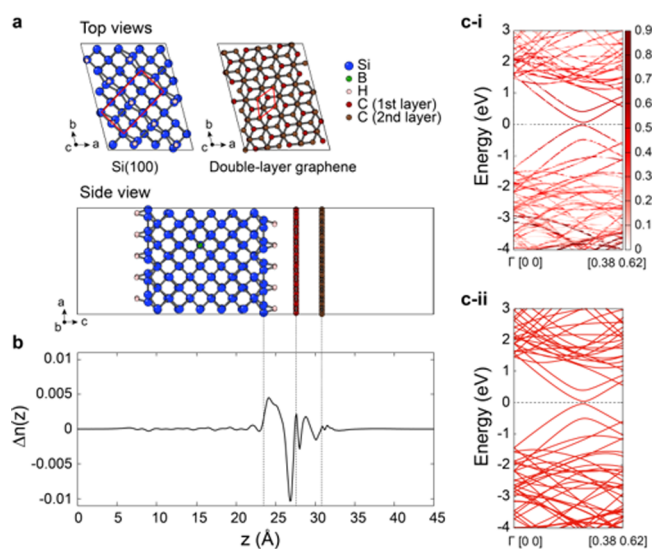


**Figure 6.** Computational modeling of p-Si/graphene junction. (a) Unit cell structure for modeling within the periodic boundary condition. Red boxes in the top views are unit cells of the reconstructed Si(100) surface and graphene. (b) The  $xy$ -plane averaged electron concentration change after junction formation. c-i (c-ii), Band structure of graphene double-layer after (before) formation of junction, and the color intensity on c-i shows the weight of C atoms.

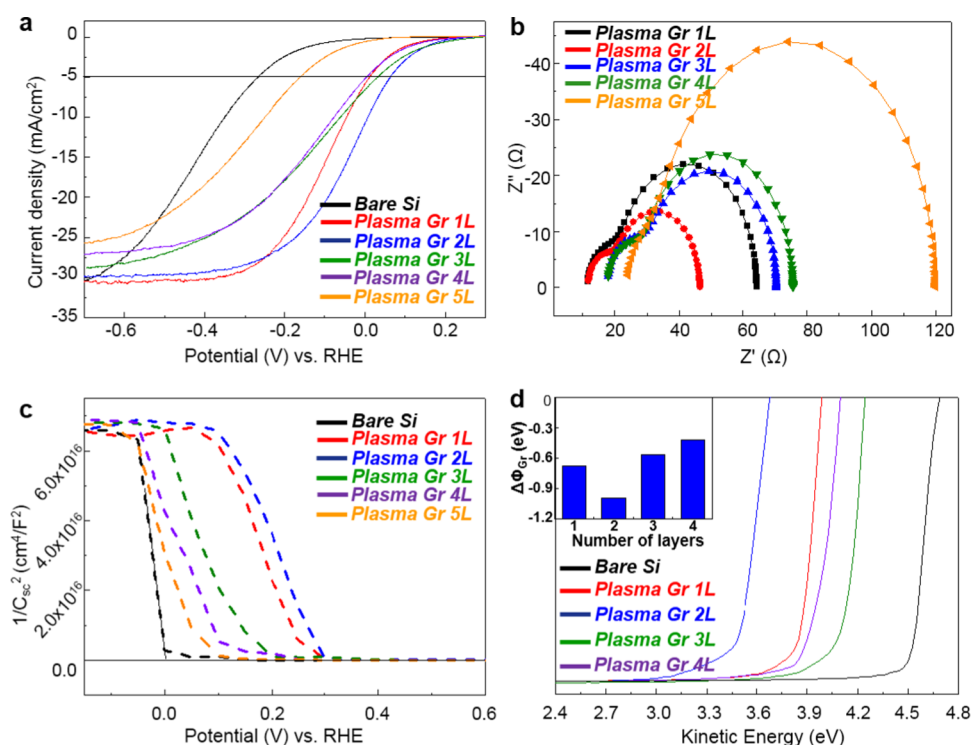


**Figure 7.** Electrochemical response of Ar plasma-treated graphene on silicon. (a)  $J$ - $E$  curves of plasma-treated multiple layers of graphene on planar p-Si. (b) Nyquist plot for plasma-treated graphene/Si electrode at 0 V vs RHE under dark conditions. (c) Mott-Schottky plots of plasma-treated graphene on Si from capacitance measurement. (d) UPS spectra of the plasma-treated graphene layer/Si electrode. Inset shows  $\Delta\Phi_G$  between plasma-treated graphene and Si surface with different numbers of graphene layers.

and p-Si. We also examined the electronic structure of double-layer graphene in the heterostructure in Figure 6c-I. By comparing with the band structure in the isolated graphene in Figure 6c-ii, one can see that the electronic structure is not affected much by the charge transfer, and the position of the Dirac point is well-preserved with respect to the Fermi level.

Compared to monolayer graphene, the value change further increased when double-layer graphene was overlaid. The change in the work function was enhanced in the case of double-layer graphene ( $-0.29$  eV). This could be due to the increased density of states, which could contribute to further Coulombic shift ( $-0.23$  eV in the double-layer). We also carried out similar calculations for multilayer graphene. The change in work function was  $-0.27$  eV for 3-layer graphene,  $-0.29$  eV for 4-layer graphene, and  $-0.28$  eV for 5-layer graphene. In this calculation, because Bernal mode stacking for multilayer graphene was assumed, the ripples and randomly titled domains that should exist in physically transferred graphenes were not considered. When graphene layers are stacked with random orientation, vertical transmission will decay exponentially as the number of graphene layers increases.<sup>48</sup> This is due to the momentum mismatch between graphene overlayers,<sup>49</sup> thus hinders charge transfer to reduce work function as graphene film gets thick. However, this trend quite nicely explains that change in work function is related to charge transfer and that compared to monolayer, multilayered graphene further increases charge transfer more.

To further enhance the HER properties of the graphene catalyst, plasma treatment was introduced to the pristine graphene layer. Plasma treatment can easily affect the intrinsic properties of graphene and produce large quantities of defects/edges.<sup>3</sup> Graphene on Cu foil was exposed to argon plasma

(10W RF power) for four seconds under 120 mTorr. This treatment was repeated for each layer in the stacking process mentioned above to obtain plasma-treated multilayer graphene. Figure S9 shows AFM images of plasma-treated graphene, showing that surface roughness clearly increases with the number of layers because of the formation of wrinkles, ripples, and folded areas. After exposure to argon plasma, structural defects at the edges of graphene causes the D peak to be significantly higher, and the G and 2D peaks rise together (Figure S9e).<sup>50</sup> Each layer of plasma-treated graphene showed decreased optical transmittance (approximately 2.15%/layer) while still being higher than that for untreated graphene layers (Figure S9f). As shown in Figures 7a and S10, under illumination, there was an additional positive shift of the overall  $J$ - $E$  curve in plasma-treated graphene. In the case of plasma-treated double-layer graphene, the PEC performance demonstrated an efficiency of 0.32%, which is 64 times higher than that of bare p-type Si. This is the highest recorded value for carbon-based catalysts on planar p-Si photocathodes (Figure S3). The  $E_{fb}$  of double-layer graphene also increased to 0.30 V vs RHE, which is higher than that of pristine double-layer graphene (0.26 V vs RHE).

To identify the source of the enhanced photoresponse and electrochemical performance of plasma-treated graphene, UPS measurements were performed. The work functions of Si and plasma-treated graphene/Si are shown in Figure 7d. Interestingly, the work functions of the plasma-treated graphene/Si electrodes were much smaller than those of untreated graphene/Si electrodes. Plasma-treated graphene contains a large quantity of defects and edges, which enables protons in the electrolyte to easily adsorb onto active sites.<sup>51</sup> Aqueous protons have been reported to easily adsorb into the atomic

defect sites in graphene because of a low kinetic energy barrier.<sup>52</sup> Another previous study has also indicated that graphene with adsorbed protium atoms (or protons in the electrolyte) exhibits an upward shift of  $E_F$  (i.e., a smaller  $E_F$ ) because adsorbed protium atoms were found to alter electronegativity within the graphene; less-electronegative protium atoms were found to behave in a manner similar to electron donors.<sup>53</sup> Specifically, our UPS measurements showed plasma-treated double-layer graphene/Si to have the lowest work function ( $\Delta\Phi_{Gr} = -1.0$  eV). These results indicate that surface modification with graphene changes the band bending of the Si surface and enhances the kinetics of hydrogen production. In this study, our PEC results and electrochemical analysis show that plasma treatment of a graphene structure on Si generates defects that improve catalytic activity.

## CONCLUSIONS

We designed heterostructures with mono-, double-, and multilayers of graphene on Si to obtain enhanced PEC performance, and we investigated the layer dependence of HER catalysis. Double-layer graphene significantly increased photon-to-current conversion efficiency. Moreover, plasma-treated double-layer graphene had a large number of defects and active sites, which further improved PEC performance up to 0.32%. On the basis of our in-depth electrochemical analysis, the low charge-transfer resistance of double-layer graphene/Si was found to give rise to a high photocurrent response for the HER. The junction effect in the double-layer graphene/Si structure also induced the strongest bending of the conduction band edge, thereby improving the likelihood that the photogenerated electrons would participate in the hydrogen-production reaction. We believe that our study provides a new and important approach to developing metal-free carbon-based catalysts for PEC hydrogen production.

## EXPERIMENTAL SECTION

**Synthesis of Graphene Layers.** Monolayer graphene was synthesized using thermal CVD. First, a copper (Cu) foil ( $10 \times 10$  cm<sup>2</sup>) was placed in a quartz tube and heated to 1000 °C for 60 min with flowing H<sub>2</sub> at 10 sccm. Then, a gas mixture of 45 sccm CH<sub>4</sub> and 10 sccm H<sub>2</sub> flowed for 30 min under 10 Torr. After 30 min, the heater was turned off and removed from the Cu foil. Next, to handle the monolayer graphene on the front side of the Cu foil, a protective layer of poly(methyl methacrylate) (PMMA) was spin-coated on the graphene on the front side of the Cu foil, and the graphene on the back was removed using oxygen plasma (100 W RF power, 12 s). Then, the PMMA film on the graphene was removed using acetone, and the remaining Cu was etched away using a 0.1 M ammonium persulfate solution. Finally, the monolayer graphene was rinsed in deionized water and transferred onto a p-type silicon substrate without a silicon oxide layer. For the various stacked graphene layers, graphene with PMMA was floated on deionized water and transferred onto another graphene layer on Cu and etched/rinsed again. The transfer and etching/rinsing procedure was repeated for up to 4 layers of graphene. To synthesize graphene with defects, the monolayer graphene on the back side of the copper was removed using oxygen plasma, and the graphene on the front side of the Cu was treated with argon plasma (10 W RF power, 4 s). The PMMA layer was coated onto this graphene, and the Cu foil was removed. Then, the treated graphene was transferred onto silicon or used in the stacking process.

**Preparation of Si Photocathode.** Boron-doped (p-type) single-crystal Si wafers (4 in. diameter, 500  $\mu$ m thickness, doped to achieve a resistivity of 10–15  $\Omega$ -cm, oriented along the (100) plane) were purchased from Namkang Co., Ltd. The wafers were cut into 1 cm<sup>2</sup> pieces and successively cleaned in acetone, 2-propanol, and deionized

water for 10 min with sonication. To establish an Ohmic contact between copper wire and the unpolished back side of the Si wafer, a gallium–indium eutectic alloy (Ga:In = 75.5:24.5, Kojundo Chemical Laboratory Co., Ltd.) was incorporated, followed by a silver paste. Epoxy was used to insulate and protect the back contact of the Si, except for the intended illumination area (0.25 cm<sup>2</sup>) on the front side of the Si. Graphene was transferred onto the Si surface from the Cu foil. PMMA was spin-coated onto the graphene, and the Cu foil was removed using an ammonium persulfate solution. After washing with deionized water, the graphene was transferred onto the Si substrate, and the PMMA was removed after soaking in acetone for 30 min.

**PEC Measurements.** A 300 W Xe lamp (Oriel) with a water filter was used as a light source with an Air Mass 1.5 Global glass filter (Newport Co., model #81094). During photocurrent measurement, light intensity was carefully maintained at 100 mW/cm<sup>2</sup> using an optical power meter (Newport, Model 1916-R). PEC measurements were performed in a three-electrode cell using an electrochemical analyzer (CHI 760E, CH Instruments, Inc.). A schematic illustration and photographs of the HER on the graphene/Si photocathode are shown in Figure S1. To minimize hydrogen bubbles adhering to the planar Si surface, the electrolyte was stirred during measurement, without the introduction of an additional surfactant. Pt wire was used as the counter electrode, and an Ag/AgCl/3 M KCl electrode was used as the reference electrode. The reference electrode was carefully calibrated with respect to RHE at 25 °C in a 1 M perchloric acid aqueous solution saturated with high-purity H<sub>2</sub>. The RHE was calibrated to  $-0.201$  V vs the Ag/AgCl reference electrode.

**Electrochemical AC Impedance Spectroscopy Measurement.** Electrochemical AC impedance spectroscopy (EIS) was performed at 0 V vs RHE under an illumination intensity of 100 mW/cm<sup>2</sup> with a frequency range of 1–10<sup>6</sup> Hz and an amplitude of 5 mV in a three-electrode cell. From the Nyquist plot, an equivalent circuit was designed to analyze the EIS spectra (Figure S8). In the equivalent circuit,  $R_{\text{overall}}$  is the overall series resistance of the circuit.  $R_1$  is the charge-transfer resistance and  $C_1$  is the capacitance phase element of the electrical double layer at the interface between the electrode and electrolyte.  $R_2$  is the charge-transfer resistance, and  $C_2$  is the capacitance phase element of the depletion layer in graphene/Si.

**Characterization.** Raman spectra were measured at room temperature with a Renishaw spectrometer at 514 nm using an Ar laser. The spot diameter was  $\sim 2$   $\mu$ m, and a 50x objective lens was used. UPS spectra were recorded using a PHI 5000 Versa Probe (ULVAC-PHI) system. The surface morphologies of the graphene films were investigated using AFM (Park system, Xe-100). Images of the graphene layer were obtained via TEM (FEI-CM20) operated at 200 keV.

**DFT Calculation.** Density functional theory (DFT) calculations were performed using the Vienna Ab-initio simulation package (VASP) code,<sup>54</sup> utilizing projected augmented wave (PAW) pseudopotential<sup>55</sup> and generalized gradient approximation (GGA).<sup>56</sup> van der Waals interactions were considered by following the DFT-D2 Grimme method.<sup>57</sup> The cutoff energy for the plane-wave basis set was chosen to be 400 eV, and the k-space was sampled on the gamma-centered  $6 \times 6 \times 1$  grid. Atomic positions were relaxed until the forces were reduced below 0.02 eV/Å. Dipole correction was included. The model system shown in Figure 6a contains 120 Si atoms and 54 C atoms. The reconstructed ( $2 \times 1$ )-Si(100) surfaces were passivated with H atoms. A B atom was substituted for one of the 120 Si atoms to emulate p-type Si.

## ASSOCIATED CONTENT

### Supporting Information

The Supporting Information is available free of charge on the ACS Publications website at DOI: 10.1021/acsami.6b11750.

Schematic illustration of hydrogen evolution reaction, spatially resolved Raman mapping, the stability test, electrochemical activity of graphene, list of performances of reported catalysts on p-Si, results obtained from fitting

of the EIS data, surface characterization, and electrochemical data of plasma-treated graphene (PDF)

## AUTHOR INFORMATION

### Corresponding Authors

\*E-mail: byunghee@snu.ac.kr (B.H.H.).

\*E-mail: nkitae@snu.ac.kr (K.T.N.).

### ORCID

Ki Tae Nam: 0000-0001-6353-8877

### Author Contributions

<sup>†</sup>K.T.N. and B.H.H. designed and supervised the project. U.S. and J.M. led the project. K.T.N., B.H.H., U.S., and J.M. wrote the manuscript and performed the laboratory experiments and analyzed the results. J.L. and S.H. contributed to the theoretical modeling. J.A. assisted with electrochemical analysis. H.-Y.A. carried out TEM imaging. D.J.K. and I.J. assisted with material analysis. C.J. carried out UPS analysis and helped with surface analysis. All authors have given approval to the final version of the manuscript. These authors contributed equally to this work.

### Notes

The authors declare no competing financial interest.

## ACKNOWLEDGMENTS

This research was supported by the Global Frontier R&D Program of the Center for Multiscale Energy System funded by the National Research Foundation under the Ministry of Science, ICT & Future, Korea (2012M3A6A7054855), by KIST Institutional Program (0543-20160004). This research was also supported by the Pioneer Research Center Program (NRF-2011-0021021) and the Basic Science Research Program (2012M3A7B4049807) through the National Research Foundation of Korea funded by the Ministry of Science, ICT & Future, Korea, by the Korean Basic Science Institute (KBSI) research Grant No. E36800.

## REFERENCES

- (1) Walter, M. G.; Warren, E. L.; McKone, J. R.; Boettcher, S. W.; Mi, Q.; Santori, E. A.; Lewis, N. S. Solar Water Splitting Cells. *Chem. Rev.* **2010**, *110* (11), 6446–6473.
- (2) Hou, Y.; Abrams, B. L.; Vesborg, P. C. K.; Björketun, M. E.; Herbst, K.; Bech, L.; Setti, A. M.; Damsgaard, C. D.; Pedersen, T.; Hansen, O.; Rossmeisl, J.; Dahl, S.; Nørskov, J. K.; Chorkendorff, I. Bioinspired Molecular Co-catalysts Bonded to a Silicon Photocathode for Solar Hydrogen Evolution. *Nat. Mater.* **2011**, *10* (6), 434–438.
- (3) Kim, Y.; Shin, D.; Chang, W. J.; Jang, H. L.; Lee, C. W.; Lee, H.-E.; Nam, K. T. Hybrid Z-Scheme Using Photosystem I and BiVO<sub>4</sub> for Hydrogen Production. *Adv. Funct. Mater.* **2015**, *25* (16), 2369–2377.
- (4) Jin, K.; Park, J.; Lee, J.; Yang, K. D.; Pradhan, G. K.; Sim, U.; Jeong, D.; Jang, H. L.; Park, S.; Kim, D.; Sung, N.-E.; Kim, S. H.; Han, S.; Nam, K. T. Hydrated Manganese(II) Phosphate (Mn<sub>3</sub>(PO<sub>4</sub>)<sub>2</sub>·3H<sub>2</sub>O) as a Water Oxidation Catalyst. *J. Am. Chem. Soc.* **2014**, *136* (20), 7435–7443.
- (5) Yin, Z.; Chen, B.; Bosman, M.; Cao, X.; Chen, J.; Zheng, B.; Zhang, H. Au Nanoparticle-Modified MoS<sub>2</sub> Nanosheet-Based Photoelectrochemical Cells for Water Splitting. *Small* **2014**, *10* (17), 3537–3543.
- (6) Zheng, Y.; Jiao, Y.; Li, L. H.; Xing, T.; Chen, Y.; Jaroniec, M.; Qiao, S. Z. Toward Design of Synergistically Active Carbon-Based Catalysts for Electrocatalytic Hydrogen Evolution. *ACS Nano* **2014**, *8* (5), 5290–5296.
- (7) Sim, U.; Yang, T.-Y.; Moon, J.; An, J.; Hwang, J.; Seo, J.-H.; Lee, J.; Kim, K. Y.; Lee, J.; Han, S.; Hong, B. H.; Nam, K. T. N-doped Monolayer Graphene Catalyst on Silicon Photocathode for Hydrogen Production. *Energy Environ. Sci.* **2013**, *6* (12), 3658–3664.

(8) Li, Y.; Wang, H.; Xie, L.; Liang, Y.; Hong, G.; Dai, H. MoS<sub>2</sub> Nanoparticles Grown on Graphene: An Advanced Catalyst for the Hydrogen Evolution Reaction. *J. Am. Chem. Soc.* **2011**, *133* (19), 7296–7299.

(9) Tian, J.; Liu, Q.; Asiri, A. M.; Alamry, K. A.; Sun, X. Ultrathin Graphitic C<sub>3</sub>N<sub>4</sub> Nanosheets/Graphene Composites: Efficient Organic Electrocatalyst for Oxygen Evolution Reaction. *ChemSusChem* **2014**, *7* (8), 2125–2130.

(10) Liang, Y.; Li, Y.; Wang, H.; Zhou, J.; Wang, J.; Regier, T.; Dai, H. Co<sub>3</sub>O<sub>4</sub> Nanocrystals on Graphene as a Synergistic Catalyst for Oxygen Reduction Reaction. *Nat. Mater.* **2011**, *10* (10), 780–786.

(11) Zheng, Y.; Jiao, Y.; Zhu, Y.; Li, L. H.; Han, Y.; Chen, Y.; Du, A.; Jaroniec, M.; Qiao, S. Z. Hydrogen Evolution by a Metal-free Electrocatalyst. *Nat. Commun.* **2014**, *5*, 1–7.

(12) Qiu, J.-D.; Wang, G.-C.; Liang, R.-P.; Xia, X.-H.; Yu, H.-W. Controllable Deposition of Platinum Nanoparticles on Graphene As an Electrocatalyst for Direct Methanol Fuel Cells. *J. Phys. Chem. C* **2011**, *115* (31), 15639–15645.

(13) Xiang, Q.; Yu, J.; Jaroniec, M. Graphene-based Semiconductor Photocatalysts. *Chem. Soc. Rev.* **2012**, *41* (2), 782–796.

(14) Huang, Z.; Zhong, P.; Wang, C.; Zhang, X.; Zhang, C. Silicon Nanowires/Reduced Graphene Oxide Composites for Enhanced Photoelectrochemical Properties. *ACS Appl. Mater. Interfaces* **2013**, *5* (6), 1961–1966.

(15) Huang, X.; Qi, X.; Boey, F.; Zhang, H. Graphene-based Composites. *Chem. Soc. Rev.* **2012**, *41* (2), 666–686.

(16) Ma, C.-B.; Qi, X.; Chen, B.; Bao, S.; Yin, Z.; Wu, X.-J.; Luo, Z.; Wei, J.; Zhang, H.-L.; Zhang, H. MoS<sub>2</sub> Nanoflower-decorated Reduced Graphene Oxide Paper for High-performance Hydrogen Evolution Reaction. *Nanoscale* **2014**, *6* (11), 5624–5629.

(17) Bae, S.; Kim, H.; Lee, Y.; Xu, X.; Park, J.-S.; Zheng, Y.; Balakrishnan, J.; Lei, T.; Ri Kim, H.; Song, Y. I.; Kim, Y.-J.; Kim, K. S.; Ozyilmaz, B.; Ahn, J.-H.; Hong, B. H.; Iijima, S. Roll-to-roll Production of 30-in. Graphene Films for Transparent Electrodes. *Nat. Nanotechnol.* **2010**, *5* (8), 574–578.

(18) Bonaccorso, F.; Sun, Z.; Hasan, T.; Ferrari, A. C. Graphene Photonics and Optoelectronics. *Nat. Photonics* **2010**, *4* (9), 611–622.

(19) Ryu, S.; Han, M. Y.; Maultzsch, J.; Heinz, T. F.; Kim, P.; Steigerwald, M. L.; Brus, L. E. Reversible Basal Plane Hydrogenation of Graphene. *Nano Lett.* **2008**, *8* (12), 4597–4602.

(20) Xie, B.; Yang, C.; Zhang, Z.; Zou, P.; Lin, Z.; Shi, G.; Yang, Q.; Kang, F.; Wong, C.-P. Shape-Tailorable Graphene-Based Ultra-High-Rate Supercapacitor for Wearable Electronics. *ACS Nano* **2015**, *9* (6), 5636–5645.

(21) Cao, X.; Yin, Z.; Zhang, H. Three-dimensional Graphene Materials: Preparation, Structures and Application in Supercapacitors. *Energy Environ. Sci.* **2014**, *7* (6), 1850–1865.

(22) Zhu, J.; Yang, D.; Yin, Z.; Yan, Q.; Zhang, H. Graphene and Graphene-Based Materials for Energy Storage Applications. *Small* **2014**, *10* (17), 3480–3498.

(23) Yin, Z.; Zhu, J.; He, Q.; Cao, X.; Tan, C.; Chen, H.; Yan, Q.; Zhang, H. Graphene-Based Materials for Solar Cell Applications. *Adv. Energy Mater.* **2014**, *4* (1), 130057410.1002/aenm.201300574

(24) Sim, U.; Moon, J.; An, J.; Kang, J. H.; Jerng, S. E.; Moon, J.; Cho, S.-P.; Hong, B. H.; Nam, K. T. N-doped Graphene Quantum Sheets on Silicon Nanowire Photocathodes for Hydrogen Production. *Energy Environ. Sci.* **2015**, *8* (4), 1329–1338.

(25) Sim, U.; Jin, K.; Oh, S.; Jeong, D.; Moon, J.; Oh, J.; Nam, K. T. Hydrogen Production by Electrolysis and Photoelectrochemical System. In *Handbook of Clean Energy Systems*; John Wiley & Sons, Ltd: New York, 2015; Vol. 5, pp 1–42.

(26) Zhang, Y.; Tang, T.-T.; Girit, C.; Hao, Z.; Martin, M. C.; Zettl, A.; Crommie, M. F.; Shen, Y. R.; Wang, F. Direct Observation of a Widely Tunable Bandgap in Bilayer Graphene. *Nature* **2009**, *459* (7248), 820–823.

(27) Lui, C. H.; Li, Z.; Mak, K. F.; Cappelluti, E.; Heinz, T. F. Observation of an Electrically Tunable Band Gap in Trilayer Graphene. *Nat. Phys.* **2011**, *7* (12), 944–947.

- (28) Khan, M. F.; Iqbal, M. Z.; Iqbal, M. W.; Eom, J. Improving the Electrical Properties of Graphene Layers by Chemical Doping. *Sci. Technol. Adv. Mater.* **2014**, *15* (5), 055004.
- (29) Ihm, K.; Lim, J. T.; Lee, K.-J.; Kwon, J. W.; Kang, T.-H.; Chung, S.; Bae, S.; Kim, J. H.; Hong, B. H.; Yeom, G. Y. Number of Graphene Layers as a Modulator of the Open-circuit Voltage of Graphene-based Solar Cell. *Appl. Phys. Lett.* **2010**, *97* (3), 032113.
- (30) Zhu, W.; Perebeinos, V.; Freitag, M.; Avouris, P. Carrier Scattering, Mobilities, and Electrostatic Potential in Monolayer, Bilayer, and Trilayer Graphene. *Phys. Rev. B: Condens. Matter Mater. Phys.* **2009**, *80* (23), 235402.
- (31) Dang, X.; Dong, H.; Wang, L.; Zhao, Y.; Guo, Z.; Hou, T.; Li, Y.; Lee, S.-T. Semiconducting Graphene on Silicon from First-Principles Calculations. *ACS Nano* **2015**, *9* (8), 8562–8568.
- (32) Valota, A. T.; Kinloch, I. A.; Novoselov, K. S.; Casiraghi, C.; Eckmann, A.; Hill, E. W.; Dryfe, R. A. W. Electrochemical Behavior of Monolayer and Bilayer Graphene. *ACS Nano* **2011**, *5* (11), 8809–8815.
- (33) Brownson, D. A. C.; Varey, S. A.; Hussain, F.; Haigh, S. J.; Banks, C. E. Electrochemical Properties of CVD Grown Pristine Graphene: Monolayer- vs. Quasi-graphene. *Nanoscale* **2014**, *6* (3), 1607–1621.
- (34) Ambrosi, A.; Pumera, M. Electrochemistry at CVD Grown Multilayer Graphene Transferred onto Flexible Substrates. *J. Phys. Chem. C* **2013**, *117* (5), 2053–2058.
- (35) Nielander, A. C.; Bierman, M. J.; Petrone, N.; Strandwitz, N. C.; Ardo, S.; Yang, F.; Hone, J.; Lewis, N. S. Photoelectrochemical Behavior of n-Type Si(111) Electrodes Coated With a Single Layer of Graphene. *J. Am. Chem. Soc.* **2013**, *135* (46), 17246–17249.
- (36) Ferrari, A. C.; Meyer, J. C.; Scardaci, V.; Casiraghi, C.; Lazzeri, M.; Mauri, F.; Piscanec, S.; Jiang, D.; Novoselov, K. S.; Roth, S.; Geim, A. K. Raman Spectrum of Graphene and Graphene Layers. *Phys. Rev. Lett.* **2006**, *97* (18), 187401.
- (37) Chen, Z.; Jaramillo, T. F.; Deutsch, T. G.; Kleiman-Shwarscstein, A.; Forman, A. J.; Gaillard, N.; Garland, R.; Takanabe, K.; Heske, C.; Sunkara, M.; McFarland, E. W.; Domen, K.; Miller, E. L.; Turner, J. A.; Dinh, H. N. Accelerating Materials Development for Photoelectrochemical Hydrogen Production: Standards for Methods, Definitions, and Reporting Protocols. *J. Mater. Res.* **2010**, *25* (01), 3–16.
- (38) Merki, D.; Vrabel, H.; Rovelli, L.; Fierro, S.; Hu, X. Fe, Co, and Ni Ions Promote the Catalytic Activity of Amorphous Molybdenum Sulfide Films for Hydrogen Evolution. *Chem. Sci.* **2012**, *3* (8), 2515–2525.
- (39) Bard, A. J.; Faulkner, L. R. *Electrochemical Methods: Fundamentals and Applications*; John Wiley & Sons, Inc.: New York, 2001, 864.
- (40) Lewis, N. S. A Quantitative Investigation of the Open-Circuit Photovoltage at the Semiconductor/Liquid Interface. *J. Electrochem. Soc.* **1984**, *131* (11), 2496–2503.
- (41) Lopes, T.; Andrade, L.; Ribeiro, H. A.; Mendes, A. Characterization of Photoelectrochemical Cells for Water Splitting by Electrochemical Impedance Spectroscopy. *Int. J. Hydrogen Energy* **2010**, *35* (20), 11601–11608.
- (42) Bott, A. W. Electrochemistry of Semiconductors. *Curr. Sep.* **1998**, *17* (3), 87–91.
- (43) Gelderman, K.; Lee, L.; Donne, S. W. Flat-Band Potential of a Semiconductor: Using the Mott–Schottky Equation. *J. Chem. Educ.* **2007**, *84* (4), 685.
- (44) Randin, J. P.; Yeager, E. Differential Capacitance Study of Stress-Annealed Pyrolytic Graphite Electrodes. *J. Electrochem. Soc.* **1971**, *118* (5), 711–714.
- (45) Kong, D.; Wang, H.; Lu, Z.; Cui, Y. CoSe<sub>2</sub> Nanoparticles Grown on Carbon Fiber Paper: An Efficient and Stable Electrocatalyst for Hydrogen Evolution Reaction. *J. Am. Chem. Soc.* **2014**, *136* (13), 4897–4900.
- (46) Trasatti, S.; Petrii, O. A. Real Surface Area Measurements in Electrochemistry. *J. Electroanal. Chem.* **1992**, *327* (1–2), 353–376.
- (47) Han, T.-H.; Lee, Y.; Choi, M.-R.; Woo, S.-H.; Bae, S.-H.; Hong, B. H.; Ahn, J.-H.; Lee, T.-W. Extremely Efficient Flexible Organic Light-emitting Diodes with Modified Graphene Anode. *Nat. Photonics* **2012**, *6* (2), 105–110.
- (48) Kuroda, M. A.; Tersoff, J.; News, D. M.; Martyna, G. J. Conductance through Multilayer Graphene Films. *Nano Lett.* **2011**, *11* (9), 3629–3633.
- (49) Gobre, V. V.; Tkatchenko, A., Scaling Laws for Van der Waals Interactions in Nanostructured Materials. *Nat. Commun.* **2013**, *4*.10.1038/ncomms3341
- (50) Kim, D. C.; Jeon, D.-Y.; Chung, H.-J.; Woo, Y.S.; Shin, J. K.; Seo, S. The Structural and Electrical Evolution of Graphene by Oxygen Plasma-induced Disorder. *Nanotechnology* **2009**, *20* (37), 375703.
- (51) Yadav, S.; Zhu, Z.; Singh, C. V. Defect Engineering of Graphene for Effective Hydrogen Storage. *Int. J. Hydrogen Energy* **2014**, *39* (10), 4981–4995.
- (52) Aichtyl, J. L.; Unocic, R. R.; Xu, L.; Cai, Y.; Raju, M.; Zhang, W.; Sacci, R. L.; Vlasiouk, I. V.; Fulvio, P. F.; Ganesh, P.; Wesolowski, D. J.; Dai, S.; van Duin, A. C. T.; Neurock, M.; Geiger, F. M. Aqueous Proton Transfer across Single-Layer Graphene. *Nat. Commun.* **2015**, *6*, 653910.1038/ncomms7539
- (53) Eren, B.; Glatzel, T.; Kisiel, M.; Fu, W.; Pawlak, R.; Gysin, U.; Nef, C.; Marot, L.; Calame, M.; Schönenberger, C.; Meyer, E. Hydrogen Plasma Microlithography of Graphene Supported on a Si/SiO<sub>2</sub> Substrate. *Appl. Phys. Lett.* **2013**, *102* (7), 071602.
- (54) Kresse, G.; Furthmüller, J. Efficient Iterative Schemes for *Ab initio* Total-energy Calculations using a Plane-wave Basis Set. *Phys. Rev. B: Condens. Matter Mater. Phys.* **1996**, *54* (16), 11169–11186.
- (55) Blöchl, P. E. Projector Augmented-wave Method. *Phys. Rev. B: Condens. Matter Mater. Phys.* **1994**, *50* (24), 17953–17979.
- (56) Perdew, J. P.; Yue, W. Accurate and Simple Density Functional for the Electronic Exchange Energy: Generalized Gradient Approximation. *Phys. Rev. B: Condens. Matter Mater. Phys.* **1986**, *33* (12), 8800–8802.
- (57) Grimme, S. Semiempirical GGA-type Density Functional Constructed with a Long-range Dispersion Correction. *J. Comput. Chem.* **2006**, *27* (15), 1787–1799.